Extracting subcellular fibrillar alignment with error estimation: Application to microtubules

Satoru Tsugawa, Nathan Hervieux, Olivier O. Hamant, Arezki Boudaoud, Richard S. Smith, Chun-Biu Li, Tamiki Komatsuzaki

To cite this version:

Satoru Tsugawa, Nathan Hervieux, Olivier O. Hamant, Arezki Boudaoud, Richard S. Smith, et al.. Extracting subcellular fibrillar alignment with error estimation: Application to microtubules. Biophysical Journal, 2016, 110 (8), pp.1836-1844. 10.1016/j.bpj.2016.03.011 . hal-02634102

Biophysical *Journal*
Article

Biophysical Society

Extracting Subcellular Fibrillar Alignment with Error Estimation: Application to Microtubules

Satoru Tsugawa,[1] Nathan Hervieux,[2] Oliver Hamant,[2] Arezki Boudaoud,[2] Richard S. Smith,[3] Chun-Biu Li,[1,*] and Tamiki Komatsuzaki[1,*]
[1]Research Institute for Electronic Science, Hokkaido University, Sapporo 001-0020 Japan; [2]Plant Reproduction and Development Lab., INRA, CNRS, ENS Lyon, UCB Lyon 1, Université de Lyon, Lyon, France; and [3]Department of Comparative Development and Genetics, Max Planck Institute for Plant Breeding Research, Cologne, Germany

ABSTRACT The order and orientation of cortical microtubule (CMT) arrays and their dynamics play an essential role in plant morphogenesis. To extract detailed CMT alignment structures in an objective, local, and accurate way, we propose an error-based extraction method that applies to general fluorescence intensity data on three-dimensional cell surfaces. Building on previous techniques to quantify alignments, our method can determine the statistical error for specific local regions, or the minimal scales of local regions for a desired accuracy goal. After validating our method with synthetic images with known alignments, we demonstrate the ability of our method to quantify subcellular CMT alignments on images with microtubules marked with green fluorescent protein in various cell types. Our method could also be applied to detect alignment structures in other fibrillar elements, such as actin filaments, cellulose, and collagen.

INTRODUCTION

A long-standing question in developmental biology is how organs reach consistent shapes despite high variability in shape and size found at the microscopic cellular level (1–5). As cell structure and growth are closely related with the dynamical behaviors of fibrillar elements, such as the cytoskeleton and the extracellular matrix, part of the answer may lie at this scale. In particular, to understand cellular variability and possible coordination mechanisms in plant development, cortical microtubules (CMTs) have received a lot of attention (6–12) because of their essential role in guiding the deposition of cellulose microfibril networks (13,14) responsible for the main load-bearing components of the cell wall. For instance, the depolymerization of microtubules leads to isotropic growth (15,16), because it results in a randomized deposition of cellulose in the cell wall, thus with isotropic elastic properties. On the other hand, it was found that organ shape and growth prescribe a mechanical stress pattern on the cell wall that can channel and modify CMT orientations (12,17). Although the analysis of microtubule behavior in multicellular development has been performed at cellular resolution, a large array of experiments and models show that microtubule behavior within a cell can be heterogeneous and dynamic (18–20). Furthermore, there is evidence that the alignment structure of CMTs within a cell emerges from local interactions between individual microtubules (7,10,21,22). Therefore, a detailed quantification of the CMT alignment structure at both the cellular and subcellular levels, and more generally the fibrillar alignment structure, are crucial to provide better understanding of the molecular mechanisms behind morphogenesis.

Different methods have been developed for the extraction of fibrillar alignment structures. In terms of experimental techniques, optical measurements that use two polarizers placed before and after the sample along the optical path can successfully infer the main orientations of the fibrillar (e.g., collagen and cellulose) arrays in the extracellular matrix or cell wall (23,24). However, these experimental methods may not be suitable for general alignment quantification because of the requirement of special instrumentation and of their limited ability to handle heterogeneous alignment structures. On the other hand, various theoretical signal-processing approaches have been proposed to extract alignment information directly from two-dimensional (2D) fibrillar signals (sometimes even three-dimensional (3D) signals) obtained from general fluorescence-based imagings (19,25–32,34–37) (see also a brief summary in (37)). These theoretical approaches offer mathematical quantifications that go beyond a simple visual inspection of the fibrillar signals and provide computational procedures (27–29) to evaluate alignment

Submitted June 18, 2015, and accepted for publication March 7, 2016.
*Correspondence: cbli@es.hokudai.ac.jp or tamiki@es.hokudai.ac.jp
Editor: Ram Dixit.
http://dx.doi.org/10.1016/j.bpj.2016.03.011

structures from optical images. Among them is the recently developed method, termed nematic tensor analysis (NTA), originally proposed to quantify spatial organizations in liquid crystals (see supplements in (11,38)). The NTA estimates the directions of fibrils in terms of intensity gradient vectors in the images. Formulated as an eigenproblem, this method evaluates the dominant orientation and anisotropy of the fibrillar alignments in a preselected region of interest (ROI). It has been shown (11,37) that the NTA has several advantages compared with traditional stereological techniques (30–32), including its applicability to general fluorescence-based images on 3D cell surface, noise insensitivity such that no presmoothing procedure is needed. In Advantages and Limitations below, we demonstrate a detailed comparison between the NTA and one of the most commonly used stereological techniques, Fourier transform method (FTM), on 2D artificial images.

Despite the attractive features of NTA, the full power of NTA is impeded by several limitations in its current form. Specifically, the ROIs used to evaluate the fibrillar orientation and anisotropy are usually chosen a priori, e.g., the cell region bound by the anticlinal cell wall is the most common choice of ROI to evaluate the overall CMT orientation of whole cells (11,37). This causes problems when applied to cells with larger sizes, such as hypocotyl cells (39), giant cells in the *Arabidopsis* sepal (40,41), and pavement cells with unusual cell shapes that resemble jigsaw puzzles (12,42), in which the heterogeneity of fibrillar alignments within the cell is expected to be crucial to understand the local variation of growth and mechanical properties of the cell wall at the subcellular level. Furthermore, a systematic error estimation of the evaluated fibrillar orientation and anisotropy is absent in NTA, which may also cause problems if the calculated orientation and anisotropy are subject to further statistical analyses that require the information of error rates to make quantitative statements of the system, e.g., when evaluating orientation correlations at the sub- and intracellular levels. In this study, we focus on the estimation of error in the NTA associated with the sampling error from a finite number of intensity gradient vectors in the ROI, which should be distinct from the dispersion from the mean orientation. We propose a generalized NTA to resolve both of the above problems simultaneously. Intuitively, we carefully formulated the errors originated from finite sampling of intensity gradient vectors in the ROI and asked two questions: 1) "What is the minimal scale of the ROI needed for a desired error value (the constant error description)?" and 2) "What is the corresponding error in the estimated orientation and anisotropy for the ROI (the constant scale description)?" The applications of our generalized method to several typical CMT fluorescent images reveal that the sizes of ROIs can be chosen with scales ($\lesssim\mu$m) much smaller than cell size (e.g., $\sim 10\mu\text{m} - 10^2\mu\text{m}$ for sepal giant cells), implying that our method enables the quantification of local heterogeneity and variability of CMT alignments at the subcellular level.

In this article, we show how the generalized NTA can be formulated and discuss several features using fluorescent CMT images as illustration. These features include the incorporation of error estimations, the ability to take into account different intensity contrasts in the CMT signals to evaluate nonuniform strength of CMT anisotropy, and the comparisons of constant error and scale descriptions. We then discuss the validations and limitations of our method using synthetic images mimicking actual experimental observations. Finally, we give detailed demonstrations of the ability of our method to unveil subcellular alignment structures in terms of CMT alignment quantification of various types of cells, including sepal giant cells, trichome cells, stomata, pavement cells, and hypocotyl cells.

MATERIALS AND METHODS

To introduce our generalized NTA method, we use a giant cell from an *Arabidopsis* sepal. The data of a giant cell is described by the cell surface information that is composed of mesh points covering the cell surface and detected by the 3D imaging analysis software MorphoGraphX (MGX) (43) (see Appendix A), and the fluorescence intensity at the mesh points measured by confocal laser scanning microscopy (see more experimental details in Appendices B and C). The fluorescence intensity is in arbitrary units (a.u.) (i.e., the confocal intensity value of the raw image). In Fig. 1 *a*, the fluorescence intensity of CMT of the giant cell projected on the mesh points and is shown by the color gradient (*high intensity in green and low intensity in dark*). Also, the detected mesh points on the cell wall are shown in white. Our method is applicable to both 2D and 3D fluorescence intensity image. The basic idea of the nematic tensor is that if there is a unidirectional distribution of fluorescence intensity $I(x, y)$ as schematically illustrated in Fig. 1 *b*, some CMTs should be aligned under the distribution. Therefore, the vectors along the constant intensity lines $\vec{t} = (t_x, t_y) = (-\partial I/\partial y, \partial I/\partial x)$, of which direction is perpendicular to the gradient of the distribution, correspond to the microtubule orientation. Note that we distinguish different contrasts of the intensity gradients using the unnormalized vector instead of the normalized one as in the previous method (see (11,37)). This generalization has not been reported so far, to the best of our knowledge, and we discuss it in detail in the next section. The local nematic tensor $n = \vec{t} \otimes \vec{t}$ is defined as the 2×2 symmetric matrix with components $n_{1,1} = t_x^2$, $n_{1,2} = t_x t_y$, $n_{2,1} = t_x t_y$, and $n_{2,2} = t_y^2$. The nematic tensor is calculated as the average $\langle n \rangle$ of the local nematic tensor over the ROI.

Because our aim is to extract the microtubule alignment at the subcellular level without any a priori assumption on the ROI, we select the region within a local circle of radius ε as depicted in Fig. 1 *a*. The center location of the local ε-circle is randomly selected, and we approximate the cell surface as a local plane with coordinates (x, y) around the ε-circle. Using the eigenvalues $(n_1 > n_2)$ and the unit length eigenvectors ($\vec{e}_1$ for n_1, $\vec{e}_2$ for n_2) of the nematic tensor $\langle n \rangle$ for each ε-circle, we define the anisotropy vector as $\vec{r} \equiv q\vec{e}_1$, $q = n_1 - n_2$. The length and orientation of the anisotropy vector correspond to the anisotropy and mean orientation of the microtubule alignment, respectively.

To take an example, we display the anisotropy vectors with $\varepsilon = 1$ (μm) for the two test cases, ordered and disordered CMT alignments, as the red segments in Fig. 1, *d* and *e*. These ROIs (Fig. 1, *d* and *e*) are shown in Fig. 1 *a*. The anisotropy q in the ordered case is much larger than that of the disordered case. The important addition in our method is how we determine the scale ε: we consider the sampling error for the eigenvalue problem associated with the finite number of vectors $\vec{t}$ in the local ε circle shown in Fig. 1 *c*,

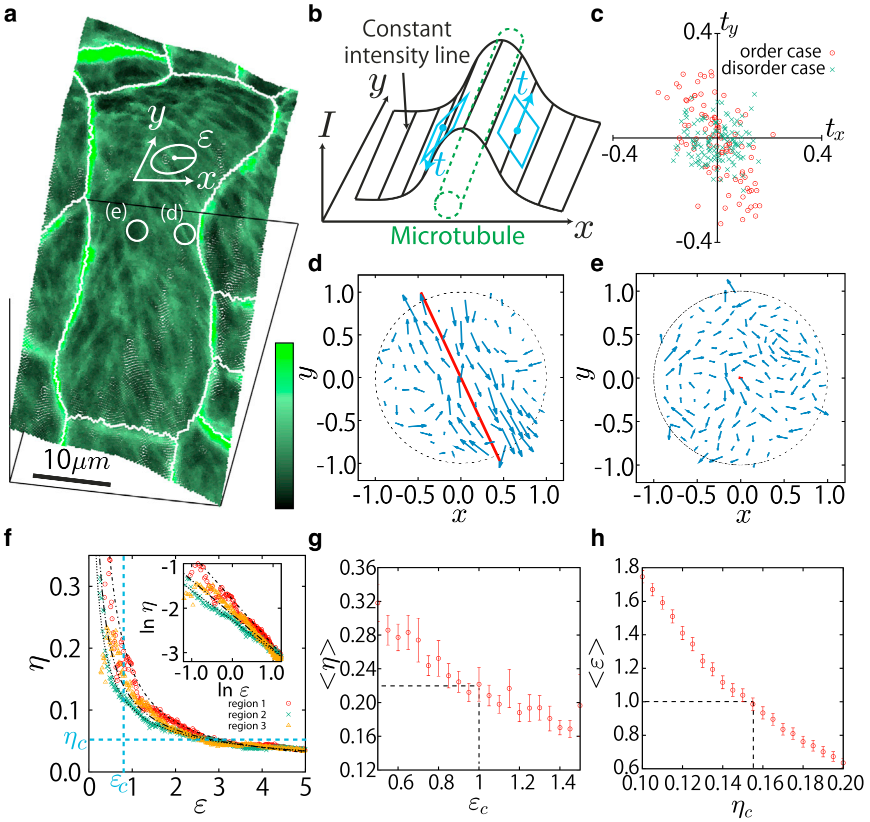

FIGURE 1 Generalization of the nematic tensor analysis. (*a*) Raw microscopy image of the CMT intensity in a giant cell is shown. The local circle of radius ε approximated locally by a plane with coordinates (x, y) is depicted. The corresponding local region for (*d*) and (*e*) are also shown. The color bar stands for the fluorescence intensity ranging from 0 to 30,000 a.u. (*b*) Schematic illustration of the concept is shown; if the intensity is unidirectionally distributed, there must be a microtubule bundle under the distribution. A vector $\vec{t}$ along the constant intensity line is also shown. (*c*) The components of the vector $\vec{t}$ of the ordered case and disordered cases are shown. (*d*) Anisotropy vector in the ordered case is shown. Blue vectors are the vectors $\vec{t}$. (*e*) Anisotropy vector in the disordered case is shown. (*f*) The error η versus the scale ε is shown for several regions. The different colors mean the randomly selected regions. (*g* and *h*) The mean error as a function of fixed scale ε_c and the mean scale as a function of fixed error η_c are shown. The mean values for both cases are calculated from 10^4 different regions, and the error bars represent the standard error. To see this figure in color, go online.

and the appropriate scale of ε is chosen by restricting the scale of the sampling error. In our study, the bootstrap method (44) that is free from any a priori assumption of noise model is used to estimate the sampling error. Using the bootstrapped distribution of (t_x, t_y), we calculate the bootstrapped anisotropy $q^{(B_k)}$ and the bootstrapped anisotropy vectors $\vec{r}^{(B_k)}$ with k ranging from 1 to the number of bootstrap trials. The deviation of the anisotropy vectors is defined as $|\delta\vec{r}|^{(B_k)} = |\vec{r} - \vec{r}^{(B_k)}|$. The meaningful "error" is estimated as the relative error $\eta = \sigma(|\delta\vec{r}|^{(B_k)}/q^{(B_k)})$, which is the standard deviation of the distribution of bootstrapped relative errors $|\delta\vec{r}|^{(B_k)}/q^{(B_k)}$ (see Appendix D for details). In Fig. 1 *f*, the relative error η is shown to decrease as a function of scale ε in several regions because the sampling number increases.

There is a trade-off to this method: if the error is fixed as η_c (or scale ε_c), the scale (or error) is distributed as in Fig. 1 *f*. Thus, depending on the purpose, we can determine appropriate fixed error or fixed scale using the mean value of η_c (or ε_c) in Fig. 1 *g* (or Fig. 1 *h*). Because the typical scale of a single microtubule bundle in our images is ~μm, we chose $\varepsilon = 1$ μm (artificially large to see the structure). The mean error for $\varepsilon_c = 1$ μm is $\langle\eta\rangle \simeq 0.222$, and the corresponding scale for $\langle\varepsilon\rangle \simeq 1$ μm is $\eta_c = 0.155$ in the current example of a giant cell. In other words, the choice of constant error description or constant scale description for the size of local ε circle can be thought as different types of "microscopes" to see the structure. To control accuracy, the error can be fixed, and to avoid losing spatial resolution, the scale can be fixed.

One of the biggest advantages of our method is the determination of the local scale (or error) by controlling the error (or scale). Among previous works (19,27–32,34–37), the traditional stereological techniques can provide the measure of accuracy in the calculation of the mean orientation of the aligned structure (30–32). The NTA has several advantages when compared with those techniques including its applicability to 3D images and noise insensitivity as mentioned above. In addition, our method provides greater information of scale where the measure of accuracy in NTA is more precise than one of the traditional stereological techniques (see the Appendix E). Error estimation with scale is essential when one considers the correlation of the locally aligned structure. For example, suppose one obtains some nonzero correlation coefficients in local regions, we need to know whether this is true correlation or artifact resulting from sampling error in the local regions.

Another advantage of our method is the option to distinguish different contrasts in the image. To demonstrate this point, we generated artificial line segments with different contrasts in Fig. S2 *a* in the Supporting Material. The line segments were created to imitate microtubule bundle images with a width of 0.1 cm, so our focusing scale was $\varepsilon \simeq 0.1$ cm. Fig. S2, *b* and *c*, shows the corresponding normalized vectors $\vec{t'} = (-\partial I/\partial y, \partial I/\partial x)/\sqrt{(\partial I/\partial x)^2 + (\partial I/\partial y)^2}$ and unnormalized vector $\vec{t} = (-\partial I/\partial y, \partial I/\partial x)$, respectively. Note that the unnormalized vectors assign different size of vectors for regions with different intensity gradients. Similarly, we used the unnormalized anisotropy $q = n_1 - n_2$ instead of the normalized anisotropy $q' = (n_1 - n_2)/(n_1 + n_2)$ to emphasize the actual strength of anisotropy $n_1 - n_2$. If we use either the normalized vector $\vec{t'}$ or the normalized anisotropy q', the results are almost the same for different contrasts of image as shown in Fig. S2, *d*-1 and *d*-2, and Fig. S2, *e*-1 and *e*-2, respectively. To distinguish the different contrasts, the use of both unnormalized vector $\vec{t}$ and unnormalized anisotropy $q = n_1 - n_2$ is required as shown in Fig. S2, *f*-1 and *f*-2. Note that the results are not strongly influenced by the choice of ε as we tested with $\varepsilon = 0.2, 0.3$ cm.

To further test the reliability of our method, we validated the procedure with another set of synthetic images with known alignments. The images contain 20 line segments that are distributed with different blurring degrees as shown in Fig. 2, *a* and *b*. The line segments are blurred with a Gaussian filter to degrade the image. The matrix size of the Gaussian filter, m, is an important blurring parameter because the degree of blurring depends on how many pixels the filter changes, i.e., $m \times m$. As the width of the line segment is roughly estimated as $m \times 0.1$ cm, the scale is fixed to 0.1 cm for all cases to see the limitation. The unit 1 cm here corresponds

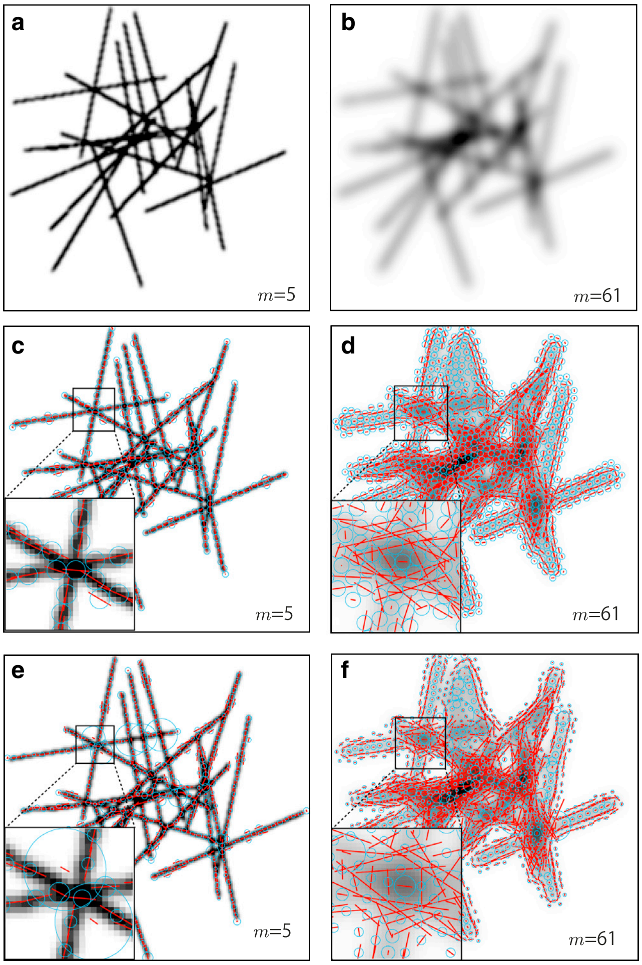

FIGURE 2 Artificial images including 20 line segments randomly located in space that show (*a*) the original artificial image in the case of the blurring parameter $m = 5$; (*b*) the original artificial image in the case of the blurring parameter $m = 61$; (*c* and *d*) the anisotropy vectors with fixed scale; and (*e* and *f*) the anisotropy vectors with fixed error. To see this figure in color, go online.

to ~10 μm in real physical scale because the imitated microtubule bundles in the image are 0.1 cm thick. Fig. 2, *c* and *d*, and Fig. 2, *e* and *f*, show the anisotropy vectors and calculated scale by red line segments and blue circles, respectively.

Next, we checked the consistency of the calculated anisotropy vectors with the original image using the deviation angle $\Delta\theta = |\theta_{\mathrm{th}} - \theta|$ with the theoretical orientation of the line segment θ_{th} and of the anisotropy vector θ depicted in Fig. 3 *a*, where only the case of constant scale is shown in Fig. 3, *a*, *c*, and *d*. Fig. 3 *d* shows that the deviation $\Delta\theta$ is larger near singular points (intersections and end points) of line segments, which implies the quantification gets worse around such singular points. Surprisingly, Fig. 3 *b* shows that the results of the deviation $\Delta\theta$ of constant scale description and constant error description are almost the same, which implies that the anisotropy vector is not strongly influenced by using ε-circles with scale around 1 μm in our imaging conditions. Note that it may not be true with other radii, so one should carefully check the sampling error in the images under consideration. In addition, our method depends on the resolution of the image, i.e., the blurring parameter m. The accuracy of the calculated anisotropy vectors, except near the singular points, decreases as a function of m, indicating that our method may not work well for extremely blurry images. In other words, to secure the accuracy of $\langle\Delta\theta/(\pi/2)\rangle = 0.2$ for instance, m needs to be ~33, as shown in Fig. 3 *b*, which means that the blurring line width should be less than 33 × 0.1 cm to achieve the accuracy of 0.2. In summary, the limitation of our method is that the quantification gets worse around singular points in the alignment structure and with decreasing resolution of the image.

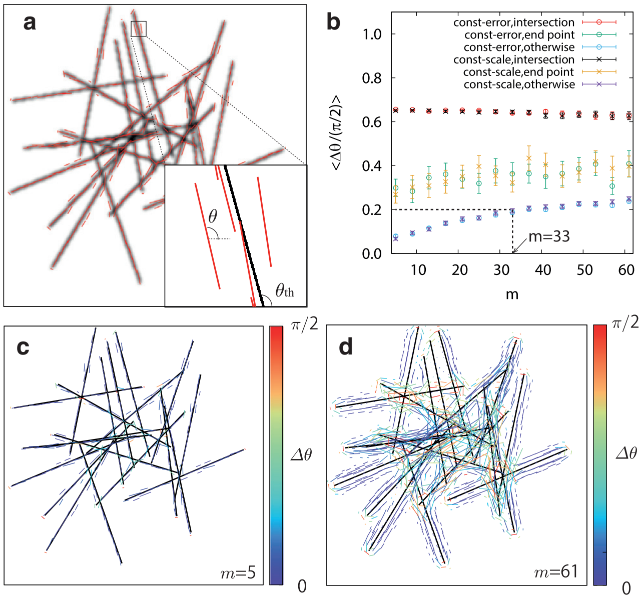

FIGURE 3 Validations and limitations of our method. (*a*) Definition of the theoretical orientation θ_{th} and the orientation of the anisotropy vector θ are shown. (*b*) The deviation angle $\Delta\theta = |\theta - \theta_{\mathrm{th}}|$ is shown as a function of the blurring parameter m. The accuracy of the anisotropy vector around singular points (intersections, end points) gets worse. The error bars represent the standard error. (*c*) The anisotropy vectors are in good agreement in the case of $m = 5$. (*d*) The anisotropy vectors around singular points have large deviation angles in the case of $m = 61$. To see this figure in color, go online.

RESULTS

We illustrate the advantages of our method compared with previous methods (11) by applying it to different types of cells. We emphasize that the novelty of the method resides in the quantification of subcellular microtubule structure with error estimation. For simplicity, we only demonstrate the constant scale case because our focusing scale is ~1 μm to see the local microtubule alignment as discussed in Materials and Methods. Fig. 4 *b* shows that our generalized method provides a more detailed structure of microtubule alignment when compared with the previously reported NTA at the cellular level in Fig. 4 *a*. Note that the results may depend on the choice of different scales or different errors, therefore the scale or error should be chosen accordingly, from the purpose of locality or accuracy.

Images sometimes contain high-intensity regions near the anticlinal cell walls because of the accumulation of fluorescence along the vertical wall as viewed from the top. In our calculation, we exclude a few layers of mesh points near the anticlinal cell wall (~1 μm) to avoid taking such signal into account. Nevertheless, we cannot always avoid such effects

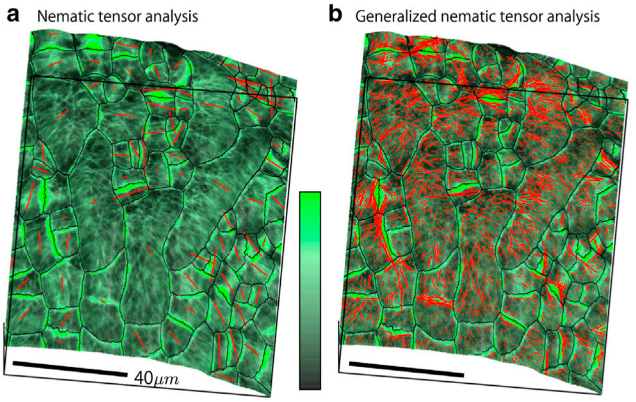

FIGURE 4 Comparison of NTA at the cellular level (*a*) and generalized NTA at the subcellular level (*b*). The color bar stands for the fluorescence intensity ranging from 0 to 30,000 a.u., and the red segments are calculated anisotropy vectors. To see this figure in color, go online.

of saturating fluorescence (see Fig. 4). In addition to the anticlinal cell wall effect, one needs to be careful about potential bias induced by cell surface curvature. Depending on the curvature of the periclinal wall and the overall orientation of the sample, the optical axis of the microscope may not always be perpendicular to the periclinal cell surface, resulting in stronger signal intensities at tilted regions because of local accumulation of fluorescence. For instance, if one cell is slightly tilted, the signal is a bit stronger on the side of the cell with the inclined wall relative to the optical axis and weaker on the flatter part (see Fig. S3).

Figs. 5, 6, S4, and S5 show the quantifications for different types of cells (giant cells, trichome (hair cell), stomata (guard cell), pavement cell, and hypocotyl). Each example is illustrated by four panels showing the raw data, the anisotropy vectors, the color plot of orientation of the anisotropy vectors, and the error in the calculation of the anisotropy vectors.

The results on giant cells show some general properties of our method. Fig. 5 *b* shows that the calculation of anisotropy vectors are in good agreement with a visual inspection of the raw data of Fig. 5 *a*. Because our method can distinguish different contrasts of the image, the anisotropy q is high for clear alignment (*white arrows*) and low for blurred regions (*black-outlined arrows*) in Fig. 5, *a* and *b*. Note that the blurred regions can reflect experimental noise or singular points (intersections or end points). We can also provide the orientation θ and the error η of the anisotropy vectors, shown respectively in Fig. 5, *c* and *d*. One can see in Fig. 5 *d* that, the smaller the anisotropy of the vector, the larger the error. This is manifested in Fig. 5 *e*, which shows that the anisotropy is negatively correlated with the error. The orientation is shown to be independent of the error in Fig. 5 *f*, which means that the calculation is not influenced by a specific orientation.

Figs. 6, S4, and S5 show the anisotropy vectors for trichome of early stage and stomata at mature stage, pavement cell, and hypocotyl cell, respectively. Figs. 6, *b–f*, S4 *b*, and S5 *b* show that the anisotropy vectors are also in good agreement with the raw data, and the white and black-outlined arrows in some figures represent strong and weak alignment, respectively. In addition, our quantification can be helpful to understand the relationship between the trichome's growth and the microtubule behaviors as discussed in (45,46). The transverse aligned structure of CMTs in guard cells is well established (see (47,48)), and the different anisotropy associated with different contrasts of the image might explain different structures. Our method is also applicable to pavement cells that are shaped like jigsaw puzzles as shown in Fig. S4. Compared with the recent studies investigating the microtubule behavior in specific areas (12), our method provides more local information of the CMT structure around lobes and necks. One can find another example of hypocotyl in which the structure of microtubules is either a right- or left-handed spiral arranged along the long axis of the hypocotyl cells as shown in Fig. S5.

DISCUSSION

The identification of microtubule regulators raises a number of important questions relating to their biochemical function in the cell and their role in morphogenesis. However to go beyond a qualitative assessment, such work requires the quantitative assessment of the microtubule defects in the corresponding mutants. In all cases, the main difficulty in connecting the images to the biological implications is the quantification of the alignment structure at the subcellular level. By providing detailed information about the alignment structure, our method addresses this point. In addition, our method allows us to discuss the relationship between subcellular microtubule alignment and other cell features, such as local curvature, local growth rate, or direction.

Our method also provides additional information about the sampling error in the calculation and the appropriate scale to quantify alignment structures with desired error values. The determination of scale based on error estimation is meaningful not only for the accuracy of the calculation but also for the discussion of the correlation length of microtubule alignment. This viewpoint of error estimation can be incorporated into other stereological techniques in handling inhomogeneous alignment structures and fixing algorithmic parameters. The consideration of error in the data enables us to distinguish the actual biological behavior from artifacts in sampling or experimental procedure. One prospect offered by this method is to precisely quantify the correlation strength and correlation range of the microtubule alignment (from the calculated anisotropy vectors), which will be a measure of the microtubule coordination at different scales.

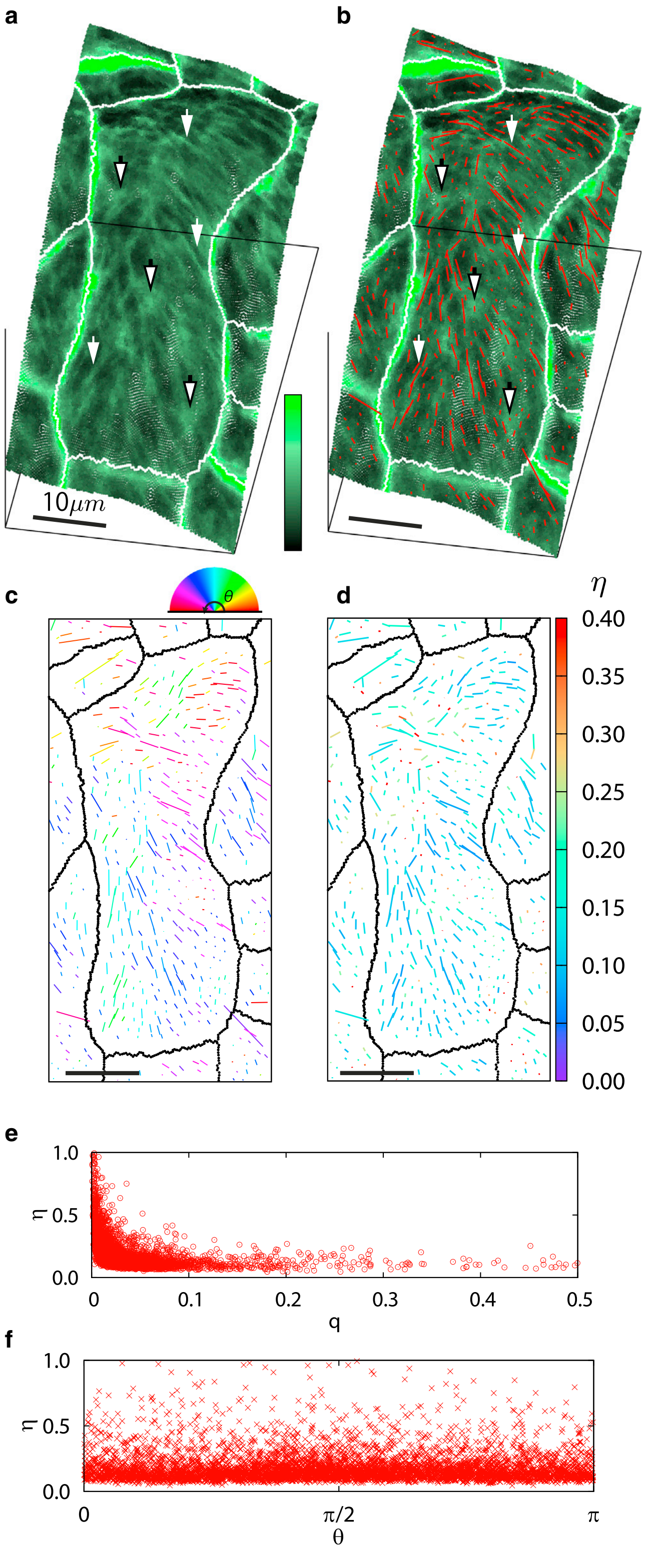

FIGURE 5 The results of anisotropy vectors for a giant cell. (*a*) Raw microscopy image of a sepal giant cell is shown. There are clear alignments (*around white arrows*) and blurred alignments (*around black-outlined arrows*). The color bars of the fluorescence intensity in this figure range from 0 to 30,000 a.u. (*b*) The local anisotropy vectors are in good agreement with (*a*). (*c*) Color plot of the orientation of the anisotropy is shown. (*d*) Heat map of the error η is shown. The color bars of the error in this figure range from 0.00 to 0.40. (*e*) The error η in anisotropy is negatively correlated with the anisotropy q. (*f*) The error in orientation is independent. To see this figure in color, go online.

APPENDIX A: VISUALIZATION SOFTWARE: MORPHOGRAPHX

We used a newly developed 3D imaging analysis software package “MorphoGraphX”(MGX), which detects cell surface geometry and the location of cells, performs cell lineage tracking, and so on (49–51). Using MGX, we first detected the surface and created the mesh from the raw confocal image as in Fig. S1 *a*, which is shown as small triangles on the surface of the sepal in Fig. S1 *b*. The coordinates of the mesh points (the vertices of the small triangles) are defined as (x, y, z). Note that some parameters were chosen in the meshing process, such as the degrees of blurring the image and smoothing the surface. We selected the distance between two neighboring mesh points as ~0.1 μm because this scale is small enough compared with cell sizes. Then, we carefully assigned the cell label n to each cell by comparing it with the original confocal image in Fig. S1 *c*. Because we are interested in seeing the CMTs, i.e., the microtubules close to the surface as shown in Fig. S1 *d*, we projected only the intensity within the depth h to the surface depicted in Fig. S1 *e*. Thus, we have a five-value data set, i.e., (x, y, z, n, I).

APPENDIX B: PLANT MATERIAL AND GROWTH CONDITIONS

We used plants labeled with microtubule marker allowing for the visualization of the microtubule network, and with membrane marker allowing for the visualization of the plasma membrane to delimit each cell and facilitate the segmentation. To visualize microtubules we used plants containing the *p35S::GFP-MBD* (WS-4) construct as described previously (17). The membrane reporter line *pUQ10::LTi6B-Mcherry* (Col-0) was provided by Yvon Jaillais. Plants were grown on soil in a phytotron in short-day conditions (8 h/16 h, light/dark periods) for 4 weeks and then transferred to long-day conditions (16 h/8 h, light/dark periods).

APPENDIX C: IMAGING

To image sepals, 1 to 2 cm long main inflorescence stems were cut from the plant. To access young buds, the first 10 to 15 flowers were dissected and the stem was kept in an apex culture medium (49) supplemented with 40 nM BAP. Then 24 h after dissection, the young buds were imaged with a SP8 Laser-Scanning Confocal Microscope (Leica) using a long-distance 25× water-dipping objective (NA: 0.95). For pavement and hypocotyl cells from the cotyledons, we used 6- to 10-day-old seedling mounted in 1% agarose.

APPENDIX D: BOOTSTRAP METHOD

The bootstrap method is a simple procedure that is often called “random drawing (sampling) with replacement.” In our case, the objective is to obtain the error from the distribution of $\vec{t} = (t_x(i), t_y(i))$, where I labels different vectors along the constant intensity line in the ROI (Fig. 1). A merit of the bootstrap method is that it is free from any assumption on the distribution of $\vec{t}$. In the first step, we make a “bootstrapped” distribution of $(t_x(i), t_y(i))$, that is, $(t_x^{(B_1)}(j), t_y^{(B_1)}(j))$ with j spanning $0, \cdots, N$ where each $t_x^{(B_1)}(j)$ and $t_y^{(B_1)}(j)$ are obtained by picking a random value of i and taking the corresponding values of $t_x(i)$ and $t_y(i)$ from the original set $(t_x(i), t_y(i))$. Similarly, other bootstrapped distribution of $(t_x^{(B_2)}(j), t_y^{(B_2)}(j))$,

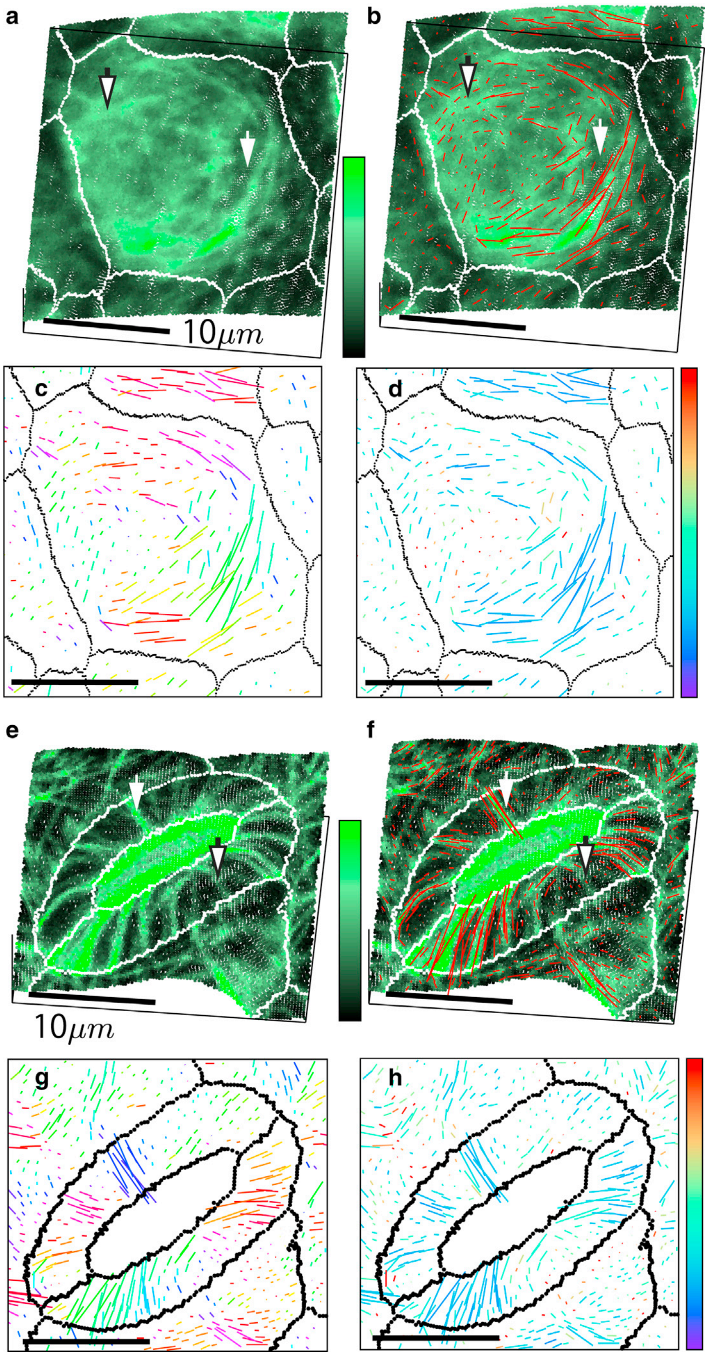

FIGURE 6 The results of anisotropy vectors for different cell types. Raw microscopy image of a young trichome (*a*) and of a stoma (*e*) are shown. There are clear alignments (*around white arrows*) and blurred alignments (*around black-outlined arrows*). The color bars of the fluorescence intensity in this figure range from 0 to 30,000 a.u. (*b* and *f*) The local anisotropy vectors are in good agreement with (*a*). (*c* and *g*) Color plots of the orientation of the anisotropy are shown. (*d* and *h*) Heat maps of the error η are shown. The color bars of the error in this figure range from 0.00 to 0.40. To see this figure in color, go online.

$(t_x^{(B_3)}(j), t_y^{(B_3)}(j)), \cdots, (t_x^{(B_M)}(j), t_y^{(B_M)}(j))$ can be generated. Because the number of bootstrap is chosen ranging from 10^2 to 10^4 in general, we used $M = 10^3$ in the current study. The result is not sensitive to the value M if M is more than 10^3. Using the bootstrapped distributions, we can calculate eigenvalues $(n_1^{(B_k)}, n_2^{(B_k)}, k = 1, \cdots, M)$, eigenvectors $(\vec{e}_1^{(B_k)}, \vec{e}_2^{(B_k)}, k = 1, \cdots, M)$, and anisotropy vectors $\vec{r}^{(B_k)} \equiv q^{(B_k)} \vec{e}^{(B_k)}$. We define the deviation of the anisotropy vectors as $|\delta \vec{r}\,|^{(B_k)} = \left|\vec{r} - \vec{r}^{(B_k)}\right|$. The relative error compared with the anisotropy $q^{(B_k)}$ is defined by $|\delta \vec{r}\,|^{(B_k)}/q^{(B_k)}$. Then, the standard deviation $\sigma(|\delta \vec{r}\,|^{(B_k)}/q^{(B_k)})$ of the distribution of relative error $|\delta \vec{r}\,|^{(B_k)}/q^{(B_k)}$ is estimated, which is called "error" in the main text.

APPENDIX E: COMPARISON WITH OTHER STEREOLOGICAL TECHNIQUES

We compare our method with three well-known techniques in traditional stereology: 1) mean intercept length (MIL) analysis, 2) line fraction techniques (LFD), and 3) Fourier transform method (FTM). It has been concluded that LFD is sensitive to anisotropy in the image and MIL is better than LFD (32,33). One study (32) concluded that the FTM is superior to MIL and LFD. Thus, we only provide in this article the comparison between FTM and our method. Fig. S6 shows that the comparison between FTM (Fig. S6 *b*) and NTA (Fig. S6 *c*) for the artificial image Fig. S6 *a*. The artificial images include twenty lines with vertical mean orientation $<\alpha> = 90^\circ$ with different angle deviation $\Delta\alpha$, i.e., $\Delta\alpha = 5^\circ$

(Fig. S6 *a*-1), $\Delta\alpha = 45^\circ$ (Fig. S6 *a*-2), and $\Delta\alpha = 90^\circ$ (Fig. S6 *a*-3). As the FTM is based on the 2D Fourier transformation of the image, FTM has several advantages, including the detection of all the frequency modes in the image, the application of filtering, etc. Fig. S6 *b* shows that the mean orientation can be detected by FTM. However, by definition, FTM is influenced by noise at high frequencies in the image. One can see that the radial power spectrum diagrams in the right panels of Fig. S6 *b* are very spiky and sensitive to high-frequency modes. Moreover, there is an assumption of homogeneous wave function that results in the disability to detect inhomogeneous alignment structures. Also, one needs to make a subjective choice of parameters such as circular filtering parameter in (31) or sector filtering parameter in (30). On the other hand, the Fig. S6 *c* shows that both the mean orientation and anisotropy of the image can be detected by NTA because of the several advantages, including less sensitivity to noise, applicability to inhomogeneous image, etc. Therefore, we concluded that the NTA is more reliable because of noise insensitivity and requires less parameters compared with FTM in the detection of anisotropy of the alignment.

SUPPORTING MATERIAL

Six figures are available at http://www.biophysj.org/biophysj/supplemental/S0006-3495(16)30060-1.

AUTHOR CONTRIBUTIONS

S.T., C.-B.L., and T.K. designed research. N.H., O.H., and A.B. performed the experiments. N.H., S.T., and R.S.S. performed the imaging analysis. S.T. and C.-B.L. analyzed the data and wrote the manuscript.

ACKNOWLEDGMENTS

We acknowledge A. H. K. Roeder, L. Hong, M. Zhu, M. Dumond, A.-L. Routier-Kierzkowska, and H. Teramoto for their valuable comments. We also thank Platim (UMS 3444 Biosciences Gerland-Lyon Sud) for help with imaging and Centre Blaise Pascal (CBP, ENS de Lyon) for help with computational analysis.

This work was supported by the Human Frontier Science Program RGP0008/2013 and ERC grant 615739 MechanoDevo.

REFERENCES

1. Dolan, L., K. Janmaat, ..., B. Scheres. 1993. Cellular organisation of the *Arabidopsis thaliana* root. *Development.* 119:71–84.
2. Melaragno, J. E., B. Mehrotra, and A. W. Coleman. 1993. Relationship between endopolyploidy and cell size in epidermal tissue of *Arabidopsis*. *Plant Cell.* 5:1661–1668.
3. Traas, J., M. Hülskamp, ..., H. Höfte. 1998. Endoreduplication and development: rule without dividing? *Curr. Opin. Plant Biol.* 1:498–503.
4. Rolland-Lagan, A.-G., J. A. Bangham, and E. Coen. 2003. Growth dynamics underlying petal shape and asymmetry. *Nature.* 422:161–163.
5. Elsner, J., M. Michalski, and D. Kwiatkowska. 2012. Spatiotemporal variation of leaf epidermal cell growth: a quantitative analysis of *Arabidopsis thaliana* wild-type and triple cyclinD3 mutant plants. *Ann. Bot. (Lond.).* 109:897–910.
6. Shaw, S. L., R. Kamyar, and D. W. Ehrhardt. 2003. Sustained microtubule treadmilling in *Arabidopsis* cortical arrays. *Science.* 300:1715–1718.
7. Dixit, R., and R. Cyr. 2004. Encounters between dynamic cortical microtubules promote ordering of the cortical array through angle-dependent modifications of microtubule behavior. *Plant Cell.* 16:3274–3284.
8. Wasteneys, G. O., and J. C. Ambrose. 2009. Spatial organization of plant cortical microtubules: close encounters of the 2D kind. *Trends Cell Biol.* 19:62–71.
9. Nakamura, M., D. W. Ehrhardt, and T. Hashimoto. 2010. Microtubule and katanin-dependent dynamics of microtubule nucleation complexes in the acentrosomal *Arabidopsis* cortical array. *Nat. Cell Biol.* 12:1064–1070.
10. Allard, J. F., G. O. Wasteneys, and E. N. Cytrynbaum. 2010. Mechanisms of self-organization of cortical microtubules in plants revealed by computational simulations. *Mol. Biol. Cell.* 21:278–286.
11. Uyttewaal, M., A. Burian, ..., O. Hamant. 2012. Mechanical stress acts via katanin to amplify differences in growth rate between adjacent cells in *Arabidopsis*. *Cell.* 149:439–451.
12. Sampathkumar, A., P. Krupinski, ..., E. M. Meyerowitz. 2014. Subcellular and supracellular mechanical stress prescribes cytoskeleton behavior in *Arabidopsis* cotyledon pavement cells. *eLife.* 3:e01967.
13. Ledbetter, M. C., and K. R. Porter. 1963. A ‘microtubule’ in plant cell fine structure. *J. Cell Biol.* 19:239–250.
14. Paredez, A. R., C. R. Somerville, and D. W. Ehrhardt. 2006. Visualization of cellulose synthase demonstrates functional association with microtubules. *Science.* 312:1491–1495.
15. Green, P. B. 1962. Mechanism for plant cellular morphogenesis. *Science.* 138:1404–1405.
16. Corson, F., O. Hamant, ..., Y. Couder. 2009. Turning a plant tissue into a living cell froth through isotropic growth. *Proc. Natl. Acad. Sci. USA.* 106:8453–8458.
17. Hamant, O., M. G. Heisler, ..., J. Traas. 2008. Developmental patterning by mechanical signals in *Arabidopsis*. *Science.* 322:1650–1655.
18. Chan, J., G. Calder, ..., C. Lloyd. 2007. Cortical microtubule arrays undergo rotary movements in *Arabidopsis* hypocotyl epidermal cells. *Nat. Cell Biol.* 9:171–175.
19. Lindeboom, J. J., M. Nakamura, ..., D. W. Ehrhardt. 2013. A mechanism for reorientation of cortical microtubule arrays driven by microtubule severing. *Science.* 342:1245533.
20. Ambrose, C., J. F. Allard, ..., G. O. Wasteneys. 2011. A CLASP-modulated cell edge barrier mechanism drives cell-wide cortical microtubule organization in *Arabidopsis*. *Nat. Commun.* 2:430.
21. Eren, E. C., R. Dixit, and N. Gautam. 2010. A three-dimensional computer simulation model reveals the mechanisms for self-organization of plant cortical microtubules into oblique arrays. *Mol. Biol. Cell.* 21:2674–2684.
22. Hawkins, R. J., S. H. Tindemans, and B. M. Mulder. 2010. Model for the orientational ordering of the plant microtubule cortical array. *Phys. Rev. E Stat. Nonlin. Soft Matter Phys.* 82:011911.
23. Green, P. B. 1960. Multinet growth in the cell wall of *Nitella*. *J. Biophys. Biochem. Cytol.* 7:289–296.
24. Tower, T. T., M. R. Neidert, and R. T. Tranquillo. 2002. Fiber alignment imaging during mechanical testing of soft tissues. *Ann. Biomed. Eng.* 30:1221–1233.
25. Karlon, W. J., J. W. Covell, ..., J. H. Omens. 1998. Automated measurement of myofiber disarray in transgenic mice with ventricular expression of *ras*. *Anat. Rec.* 252:612–625.
26. Karlon, W. J., P.-P. Hsu, ..., J. H. Omens. 1999. Measurement of orientation and distribution of cellular alignment and cytoskeletal organization. *Ann. Biomed. Eng.* 27:712–720.
27. Sugimoto, K., R. Himmelspach, ..., G. O. Wasteneys. 2003. Mutation or drug-dependent microtubule disruption causes radial swelling without altering parallel cellulose microfibril deposition in *Arabidopsis* root cells. *Plant Cell.* 15:1414–1429.
28. Wang, X., L. Zhu, ..., M. Yuan. 2007. *Arabidopsis* MICROTUBULE-ASSOCIATED PROTEIN18 functions in directional cell growth by destabilizing cortical microtubules. *Plant Cell.* 19:877–889.

29. Sainsbury, F., D. A. Collings, …, J. Marc. 2008. Developmental reorientation of transverse cortical microtubules to longitudinal directions: a role for actomyosin-based streaming and partial microtubule-membrane detachment. *Plant J.* 56:116–131.
30. Frank, C., B. MacFarlane, …, R. Bray. 1991. A quantitative analysis of matrix alignment in ligament scars: a comparison of movement versus immobilization in an immature rabbit model. *J. Orthop. Res.* 9: 219–227.
31. Marquez, J. P. 2006. Fourier analysis and automated measurement of cell and fiber angular orientation distributions. *Int. J. Solids Struct.* 43:6413–6423.
32. Sander, E. A., and V. H. Barocas. 2009. Comparison of 2D fiber network orientation measurement methods. *J. Biomed. Mater. Res. A.* 88:322–331.
33. Geraets, W. G. M. 1998. Comparison of two methods for measuring orientation. *Bone.* 23:383–388.
34. Yi, Q., and M. G. Coppolino. 2006. Automated classification and quantification of F-actin-containing ruffles in confocal micrographs. *Biotechniques.* 40:745–756.
35. Higaki, T., N. Kutsuna, …, S. Hasezawa. 2010. Quantification and cluster analysis of actin cytoskeletal structures in plant cells: role of actin bundling in stomatal movement during diurnal cycles in *Arabidopsis* guard cells. *Plant J.* 61:156–165.
36. Jacques, E., J. Buytaert, …, K. Vissenberg. 2013. MicroFilament Analyzer, an image analysis tool for quantifying fibrillar orientation, reveals changes in microtubule organization during gravitropism. *Plant J.* 74:1045–1058.
37. Boudaoud, A., A. Burian, …, O. Hamant. 2014. FibrilTool, an ImageJ plug-in to quantify fibrillar structures in raw microscopy images. *Nat. Protoc.* 9:457–463.
38. Stephen, M. J., and J. P. Straley. 1974. Physics of liquid crystals. *Rev. Mod. Phys.* 46:617.
39. Gendreau, E., J. Traas, …, H. Höfte. 1997. Cellular basis of hypocotyl growth in *Arabidopsis thaliana*. *Plant Physiol.* 114:295–305.
40. Roeder, A. H. K., V. Chickarmane, …, E. M. Meyerowitz. 2010. Variability in the control of cell division underlies sepal epidermal patterning in *Arabidopsis thaliana*. *PLoS Biol.* 8:e1000367.
41. Roeder, A. H. K., A. Cunha, …, E. M. Meyerowitz. 2012. Cell cycle regulates cell type in the *Arabidopsis* sepal. *Development.* 139:4416–4427.
42. Zhang, C., L. E. Halsey, and D. B. Szymanski. 2011. The development and geometry of shape change in *Arabidopsis thaliana* cotyledon pavement cells. *BMC Plant Biol.* 11:27.
43. Barbier de Reuille, P., A. L. Routier-Kierzkowska, …, R. S. Smith. 2015. MorphoGraphX: a platform for quantifying morphogenesis in 4D. *eLife.* 4:05864.
44. Efron, B. 1979. Bootstrap methods: another look at the jackknife. *Ann. Stat.* 7:1–26.
45. Rerie, W. G., K. A. Feldmann, and M. D. Marks. 1994. The *GLABRA2* gene encodes a homeo domain protein required for normal trichome development in *Arabidopsis*. *Genes Dev.* 8:1388–1399.
46. Mathur, J., and N.-H. Chua. 2000. Microtubule stabilization leads to growth reorientation in *Arabidopsis* trichomes. *Plant Cell.* 12:465–477.
47. Lucas, J. R., J. A. Nadeau, and F. D. Sack. 2006. Microtubule arrays and *Arabidopsis* stomatal development. *J. Exp. Bot.* 57:71–79.
48. Eisinger, W., D. Ehrhardt, and W. Briggs. 2012. Microtubules are essential for guard-cell function in *Vicia* and *Arabidopsis*. *Mol. Plant.* 5:601–610.
49. Kierzkowski, D., N. Nakayama, …, R. S. Smith. 2012. Elastic domains regulate growth and organogenesis in the plant shoot apical meristem. *Science.* 335:1096–1099.
50. Yoshida, S., P. Barbier de Reuille, …, D. Weijers. 2014. Genetic control of plant development by overriding a geometric division rule. *Dev. Cell.* 29:75–87.
51. Hamant, O., P. Das, and A. Burian. 2014. Time-lapse imaging of developing meristems using confocal laser scanning microscope. *Methods Mol. Biol.* 1080:111–119.